Phase-field approach for faceted solidification

Jean-Marc Debierre,[1] Alain Karma,[2] Franck Celestini,[3] and Rahma Guérin[1]

[1]*Laboratoire Matériaux et Microélectronique de Provence (UMR 6137), Université d'Aix-Marseille III, Faculté des Sciences et Techniques de Saint-Jérôme, Case 151, 13397 Marseille Cedex 20, France*

[2]*Department of Physics and Center for Interdisciplinary Research on Complex Systems, Northeastern University, Boston, Massachusetts 02115, USA*

[3]*Laboratoire de Physique de la Matière Condensée (UMR 6622), Université de Nice-Sophia-Antipolis, Parc Valrose, 06108 Nice Cedex 2, France*

We extend the phase-field approach to model the solidification of faceted materials. Our approach consists of using an approximate γ plot with rounded cusps that can approach arbitrarily closely the true γ plot with sharp cusps that correspond to faceted orientations. The phase-field equations are solved in the thin-interface limit with local equilibrium at the solid-liquid interface [A. Karma and W.-J. Rappel, Phys. Rev. E **53**, R3017 (1996)]. The convergence of our approach is first demonstrated for equilibrium shapes. The growth of faceted needle crystals in an undercooled melt is then studied as a function of undercooling and the cusp amplitude δ for a γ plot of the form $\gamma = \gamma_0[1 + \delta(|\sin\theta| + |\cos\theta|)]$. The phase-field results are consistent with the scaling law $\Lambda \sim V^{-1/2}$ observed experimentally, where Λ is the facet length and V is the growth rate. In addition, the variation of V and Λ with δ is found to be reasonably well predicted by an approximate sharp-interface analytical theory that includes capillary effects and assumes circular and parabolic forms for the front and trailing rough parts of the needle crystal, respectively.

I. INTRODUCTION

Over the last decade, the phase-field approach [1,2] has been developed extensively to model the solidification of both pure materials and alloys [3]. Most of the work to date has focused on the case where the excess free energy of the solid-liquid interface

$$\gamma \equiv \gamma_0 f(\theta) \qquad (1)$$

is a smooth function of the angle θ between the direction normal to the interface and some fixed crystalline axis. In particular, the simple form

$$f(\theta) = 1 + \epsilon \cos 4\theta + \cdots, \qquad (2)$$

appropriate for a weakly anisotropic material with an underlying cubic symmetry, has been widely used in studies of dendritic solidification [4–9]. For a smooth γ plot, the value of the diffusion field (dimensionless undercooling or supersaturation) at the interface is given by the standard Gibbs-Thomson condition

$$u = -d_0 \left[f + \frac{d^2 f}{d\theta^2} \right] \kappa, \qquad (3)$$

where d_0 is a microscopic capillary length (thermal or chemical) that is proportional to γ_0 and κ is the interface curvature. Dendritic growth in pure materials [6–8] and alloys [9] has been modeled quantitatively with a thin-interface limit [6] of the phase-field model that yields the boundary condition (3) and overcomes the stringent computational constraint associated with a finite interface thickness. These simulation studies modeled the common situation of a

weak anisotropy where the interface stiffness $\gamma + d^2\gamma/d\theta^2$, and hence the square bracket in Eq. (3), is everywhere positive. More recently, the phase-field approach has also been successfully extended to model strongly anisotropic equilibrium crystal shapes where the stiffness becomes negative for some range of θ [10]. In this case, which occurs for example when $\epsilon > 1/15$ for form (2) of $f(\theta)$, the slope of the interface has discontinuities that must be present to eliminate thermodynamically unstable, and hence forbidden, orientations for which the stiffness is negative.

In this paper, we extend the phase-field approach to model a wide class of materials that form facets for a discrete set of orientations. The interfacial energy is generally nonanalytic for orientations close to a facet. This nonanalyticity is reflected in the presence of cusps in the γ plot that are of the form

$$f(\theta) \approx 1 + \delta|\theta - \theta_c| + \cdots \quad \text{for} \quad |\theta - \theta_c| \ll 1, \qquad (4)$$

where $\theta = \theta_c$ is the orientation of a given facet. In the simplest model where vicinal surfaces are assumed to consist of straight ledges of height a separated by terraces of width $l \approx a/|\theta - \theta_c|$, the cusp amplitude $\delta = \gamma_L/(a\gamma_0)$ where γ_L is the ledge energy per unit length.

To a good first approximation, the tendency of a material to facet is described by Jackson's well-known α factor [11] that is the product of a dimensionless crystallographic factor that depends on the crystal structure and the orientation of the interface and the ratio of the latent heat per mole to the rare gas constant. Jackson's theory predicts that materials with $\alpha \lesssim 2$ (such as metals with low entropy of melting) will have rough interfaces, while those with $\alpha \gtrsim 2$ (such as non-

metals and compounds) will form facets, consistent with experimental observations across a wide range of materials [12].

The growth of faceted dendrites has been studied both experimentally [13,14] and theoretically in the context of a sharp-interface approach [15–17]. Experimentally, facets are seen to appear near the tip of the needle crystal that nevertheless retains a parabolic shape on the larger scale of the whole crystal that includes the trailing rough parts. From a theoretical standpoint, a main difficulty to model faceted growth is that the standard Gibbs-Thomson relation can only be applied to rough parts of the interface. On a facet, this relation takes the form of an integral condition that is obtained by making the substitution $\kappa = d\theta/ds$, where s denotes the arclength along the interface, and integrating both sides of Eq. (3) from one extremity (s_-) of the facet to the other (s_+). This integration yields the condition

$$\int_{s_-}^{s_+} u\, ds = -d_0 \left(\left. \frac{df}{d\theta} \right|_+ - \left. \frac{df}{d\theta} \right|_- \right) = -2\, d_0\, \delta, \qquad (5)$$

where $df/d\theta|_\pm$ denotes the limiting values of $df/d\theta$ on each side of the cusp ($\theta - \theta_c \to 0^\pm$).

For an equilibrium crystal with a constant undercooling or supersaturation ($u < 0$) along the interface, the above condition implies that the length Λ of the facet is simply proportional to the amplitude of the cusp

$$\Lambda = 2 \frac{d_0}{-u}\, \delta. \qquad (6)$$

For growth outside of equilibrium, the determination of the facet length and the shape of the rough parts requires in general a self-consistent solution of the free-boundary problem defined by the appropriate diffusion equations for u in solid and liquid, the standard Stefan condition of heat or mass conservation on the interface, and the local equilibrium conditions (3) and (5) on rough parts and facets, respectively.

An analytical solution to this problem was obtained for steady-state growth by Adda-Bedia and Hakim [16] in the small Péclet number limit neglecting capillary effects on the rough parts. They concluded from this analysis that it is not possible to require both tangential matching of the rough and faceted parts of the interface and the equilibrium condition ($u \approx 0$) on the front and trailing rough parts. Furthermore, they proposed an approximate solution to the full problem that includes capillary effects on the rough parts in the large δ limit. In this solution, the facets are assumed to match tangentially to a small quasicircular tip that is significantly more undercooled than the rough trailing parts. A numerical solution of the steady-state growth problem was later obtained for arbitrary δ by Adda-Bedia and Ben Amar [17] using a boundary integral method. This calculation gave results that are consistent with the approximate solution of Adda Bedia and Hakim for large δ.

At present, a phase-field approach for faceted growth would be highly desirable to study the stability of needle crystal solutions as well as to explore the full dynamical range of morphological evolution when the interface shape is nonstationary. Treating separately the rough and faceted parts of the interface appears to be difficult within a phase-field formulation. To circumvent this difficulty, we follow a procedure that is similar in spirit, but different in details, to the one introduced by Adda Bedia and Ben Amar [17] in a sharp-interface context. The basic idea is to use a regularized form of the γ plot that can approximate arbitrarily closely the γ plot with sharp cusps. The discontinuity of $df/d\theta$ at a cusp can be viewed mathematically as the stiffness behaving as a sharply peaked Dirac δ function at $\theta = \theta_c$. Therefore, different regularizations of this discontinuity can be viewed as different regularizations of this δ function peak that must satisfy the cusp condition

$$\lim_{\theta_0 \to 0} \int_{\theta_c - \theta_0}^{\theta_c + \theta_0} d\theta \left[f + \frac{d^2 f}{d\theta^2} \right] = 2\delta, \qquad (7)$$

imposed by form (4) of f near a cusp. Adda Bedia and Ben Amar have introduced regularizations in which all derivatives of the stiffness and hence f are continuous. In a phase-field context, we have found it more convenient to use a regularization where only f and its first derivative are continuous and the dimensionless stiffness $f + d^2 f/d\theta^2$ is a step function regularization of the δ function, $f + d^2 f/d\theta^2 \approx \delta/\theta_0$ for $\theta_c - \theta_0 \leq \theta \leq \theta_c + \theta_0$. In practice, computations for small θ_0 turn out to be more costly because the larger stiffness ($\approx \delta/\theta_0$) requires a smaller time step. As we shall see, however, an accurate extrapolation to the $\theta_0 \to 0$ limit is nevertheless possible.

It is important to emphasize that this paper only represents a first step in the extension of the phase-field approach to faceted materials. In this first step, we focus on capillary effects and purposely neglect the kinetic undercooling of the interface in order to relate quantitatively the phase-field results to sharp-interface theory in a well-studied limit [16,17]. Coping with the presence of cusps in the γ plot, which is the main difference between faceted and nonfaceted growth as far as capillary effects are concerned, already represents a nontrivial task that is best handled separately. In future work, we plan to build on the methodology developed in this paper to model different nonlinear relationships between a finite interface undercooling and the interface velocity, which are known to be associated with different crystal growth mechanisms (such as island nucleation and spiral growth [12]).

The phase-field model and the details of this smoothing procedure are described in the following section. The numerical implementation of the equations is then presented in Sec. III. The convergence of our numerical approach is demonstrated in Sec. IV by a detailed comparison of diffuse-interface and sharp-interface equilibrium crystal shapes. Results concerning the steady-state growth of faceted needle crystals in a pure undercooled melt are then presented in Sec. V. These results are then compared in Sec. VI to the predictions of an approximate sharp-interface theory that assumes simple forms for the front and trailing rough parts as an extension of the solution proposed in Ref. [16]. Concluding remarks and future prospects are then discussed in Sec. VI.

II. PHASE-FIELD MODEL

We consider the growth of a crystal from a pure under-cooled melt with the thermal diffusivity being the same in the solid and liquid. We follow the phase-field approach developed by Karma and Rappel [6] that has proven successful to model efficiently nonfaceted dendritic growth. We briefly recall the basic features of the phase-field model and of the thin-interface limit used to relate the phase-field and sharp-interface models.

The dimensionless temperature field is defined as $u = (T - T_M)/(L/c_p)$, where T is the temperature, T_M is the melting temperature, L is the latent heat per unit volume, and c_p is the specific heat at constant pressure per unit volume. The phase field ψ is taken to be equal to $+1$ (-1) in the solid (liquid) phase and varies continuously across the diffuse interface. In two dimensions, the time evolution of both fields is governed by the equations

$$\partial_t u = D\nabla^2 u + \tfrac{1}{2}\partial_t \psi \tag{8}$$

and

$$\tau(\theta)\partial_t \psi = [\psi - \lambda u(1-\psi^2)](1-\psi^2) + \vec{\nabla}\cdot[W(\theta)^2\vec{\nabla}\psi]$$
$$- \partial_x[W(\theta)W'(\theta)\partial_y\psi] + \partial_y[W(\theta)W'(\theta)\partial_x\psi], \tag{9}$$

where D is the thermal diffusivity, θ is the angle between the normal to the interface and the x axis, λ is a dimensionless coupling constant between the temperature and phase fields, and

$$W(\theta) \equiv W_0 f(\theta) \tag{10}$$

is the diffuse-interface thickness. In the thin-interface limit where W_0 is much smaller than the mesoscale of the growing crystal [6], the above phase-field equations reduce to the standard sharp-interface model of diffusion-limited growth with the velocity-dependent form of the Gibbs-Thomson condition

$$u = -d_0\left[f(\theta) + \frac{d^2 f(\theta)}{d\theta^2}\right]\kappa - \beta(\theta)v_n, \tag{11}$$

where

$$d_0 = \frac{a_1 W_0}{\lambda} \tag{12}$$

and

$$\beta(\theta) = \frac{a_1}{\lambda}\frac{\tau(\theta)}{W(\theta)}\left[1 - a_2\lambda\frac{W(\theta)^2}{D\tau(\theta)}\right]. \tag{13}$$

In addition, a_1 and a_2 are constants that depend generally on the choice of the double-well potential and other functions in the phase-field model. For the present choices that are the same as in Refs. [6], $a_1 = 0.8839\ldots$ and $a_2 = 0.6267\ldots$.

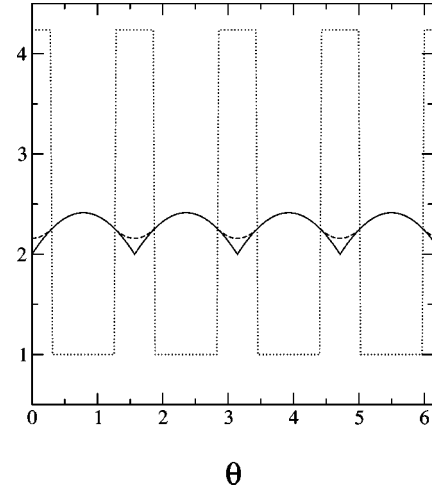To model faceted growth, we use the simplest form of the γ plot,

FIG. 1. Three functions of the interface orientation angle θ represented for a cusp amplitude $\delta = 1.0$. Solid line: anisotropy function with sharp cusps, $f(\theta)$. Dashed line: smoothed anisotropy function, $f_s(\theta)$. Dotted line: dimensionless stiffness, $f_s(\theta) + f_s''(\theta)$. A large smoothing angle $\theta_0 = \pi/10$ is used here to make the difference between f and f_s visible.

$$f(\theta) = 1 + \delta(|\sin\theta| + |\cos\theta|). \tag{14}$$

This form is directly adapted from the broken-bond model which describes satisfactorily faceted solid-gas interfaces [18]. The same form was used in previous sharp-interface calculations [16,17].

Furthermore, in order to model the limit with local equilibrium at the interface, i.e., vanishing interface kinetics $\beta(\theta) = 0$, we impose [6]

$$\tau(\theta) = \tau_0 f(\theta)^2 \tag{15}$$

and

$$\lambda = \frac{1}{a_2}\frac{D\tau_0}{W_0^2}, \tag{16}$$

which makes $\beta(\theta)$ vanish for all values of θ.

For the above choice of γ plot, the dimensionless stiffness defined by

$$S(\theta) \equiv f(\theta) + \frac{d^2 f(\theta)}{d\theta^2} \tag{17}$$

is constant except at the cusps, $\theta = \theta_{c,n} = n\pi/2$ (with n an integer), where it diverges. The discontinuities in the first derivative of the interfacial energy need to be regularized, since $f'(\theta)$ is not defined for $\theta = \theta_{c,n}$. A simple strategy to circumvent this problem is to smooth out the cusps by replacing $f(\theta)$ with a smooth function sucha as a sine in a small range of θ values around the cusps (Fig. 1). For the sake of clarity, we restrict our discussion to the first quadrant, $\theta \in [0,\pi/2]$, since the problem has a natural fourfold symmetry. The smoothed anisotropy function $f_s(\theta)$ then reads

$$f_s(\theta) = \begin{cases} 1 + \delta(\sin\theta + \cos\theta) & \text{if} \quad \theta_0 < \theta < \dfrac{\pi}{2} - \theta_0 \\[2mm] B - A\cos\theta & \text{if} \quad \theta \le \theta_0 \\[2mm] B - A\sin\theta & \text{if} \quad \theta \ge \dfrac{\pi}{2} - \theta_0, \end{cases}$$

$$(18)$$

and its derivative

$$f'_s(\theta) = \begin{cases} \delta(\cos\theta - \sin\theta) & \text{if} \quad \theta_0 < \theta < \dfrac{\pi}{2} - \theta_0 \\[2mm] A\sin\theta & \text{if} \quad \theta \le \theta_0 \\[2mm] -A\cos\theta & \text{if} \quad \theta \ge \dfrac{\pi}{2} - \theta_0. \end{cases} \quad (19)$$

The two constants A and B are obtained by expressing the continuity of f_s and f'_s at $\theta = \theta_0$,

$$A = \delta(\cot\theta_0 - 1) \qquad (20)$$

and

$$B = 1 + \delta/\sin\theta_0. \qquad (21)$$

Now $f'_s(0) = f'_s(\pi/2) = 0$ and $W(\theta)$ is no more singular in the cusp directions. Note, however, that f''_s is *not* continuous at $\theta = \theta_0$. Consequently, the dimensionless stiffness is a step function of θ (see Fig. 1),

$$S(\theta) = \begin{cases} 1 & \text{if} \quad \theta_0 < \theta < \dfrac{\pi}{2} - \theta_0 \\[2mm] 1 + \delta/\sin\theta_0 & \text{if} \quad \theta \le \theta_0 \quad \text{or} \quad \theta \ge \dfrac{\pi}{2} - \theta_0. \end{cases}$$

$$(22)$$

III. NUMERICAL IMPLEMENTATION

We now briefly describe how Eqs. (8) and (9) are discretized in our code. The interface is represented by the $\psi = 0$ contour, so that $\vec{\nabla}\psi$ is by construction collinear to the unit vector along the normal to the interface, **n**. If $|\vec{\nabla}\psi| \ne 0$, the two components of this vector are given by

$$n_x = \cos\theta = -\partial_x\psi/|\vec{\nabla}\psi| \qquad (23)$$

and

$$n_y = \sin\theta = -\partial_y\psi/|\vec{\nabla}\psi|, \qquad (24)$$

and f_s and f'_s are computed according to Eqs. (18) and (19). Conversely, when $|\vec{\nabla}\psi| = 0$, one sets

$$f_s(\theta) = 1 \qquad (25)$$

and

$$f'_s(\theta) = 0. \qquad (26)$$

Equations (25) and (26) are imposed in places where the phase-field gradient vanishes because the unit vector normal to the interface loses its meaning far from the interface. With this choice, the phase-field simply relaxes to a local minimum of the free-energy density (± 1) deep inside the liquid or solid phase, where the temperature field obeys a simple diffusion equation. Numerical simulations of Eqs. (8) and (9) are performed by implementing a finite-difference scheme on a regular square mesh with mesh size $h = 0.4W_0$. The domain considered is the quadrant $0 \le x \le Nh$ and $0 \le y \le Nh$, with N an integer. A standard first order in time Euler scheme with a time step Δt and a second order in space discretization of the spatial derivatives are used.

Let $u_{i,j}$ and $\psi_{i,j}$, respectively, denote the discretized reduced temperature and phase field at point $(x = ih, y = jh)$. In a first step, one computes $\nabla^2 u$, $\nabla^2\psi$, $\partial_x\psi$, $\partial_y\psi$, $W(\theta)W'(\theta)$, and $W(\theta)$ for each point of the extended domain, i and $j \in [-1, N+1]$, and the results are stored in six intermediate arrays. Reflecting conditions are imposed on u and ψ at all the domain boundaries (i or $j = -2, -1, N+1, N+2$), and using centered differencing approximations, we have

$$\nabla^2 u_{i,j} = [u_{i+1,j} + u_{i-1,j} + u_{i,j+1} + u_{i,j-1} - 4u_{i,j}]/h^2,$$

$$(27)$$

$$\nabla^2\psi_{i,j} = [\psi_{i+1,j} + \psi_{i-1,j} + \psi_{i,j+1} + \psi_{i,j-1} - 4\psi_{i,j}]/h^2,$$

$$(28)$$

$$\partial_x\psi_{i,j} = [\psi_{i+1,j} - \psi_{i-1,j}]/(2h), \qquad (29)$$

$$\partial_y\psi_{i,j} = [\psi_{i,j+1} - \psi_{i,j-1}]/(2h). \qquad (30)$$

The two remaining arrays $(WW')_{i,j}$ and $W_{i,j}$ are given by Eq. (10) into which f is replaced with f_s.

In the second step, one solves Eqs. (8) and (9) on the inner points of the domain, i and $j \in [0, N]$. To do so, the last three terms in Eq. (9) are written in a slightly different form,

$$W(\theta)^2\nabla^2\psi + 2W(\theta)\vec{\nabla}W(\theta)\cdot\vec{\nabla}\psi - (\partial_y\psi)\partial_x[W(\theta)W'(\theta)]$$

$$+ (\partial_x\psi)\partial_y[W(\theta)W'(\theta)], \qquad (31)$$

so that each new term can be computed with the help of the intermediate arrays. For instance, the last term is discretized as

$$(\partial_x\psi_{i,j})[(WW')_{i,j+1} - (WW')_{i,j-1}]/(2h). \qquad (32)$$

IV. EQUILIBRIUM SHAPES

A. Comparison between analytical and phase-field results

We first check our code by computing the equilibrium shape of the crystal. In thermal equilibrium, $u = -\Delta$ everywhere, and the evolution equation for the phase field reduces to
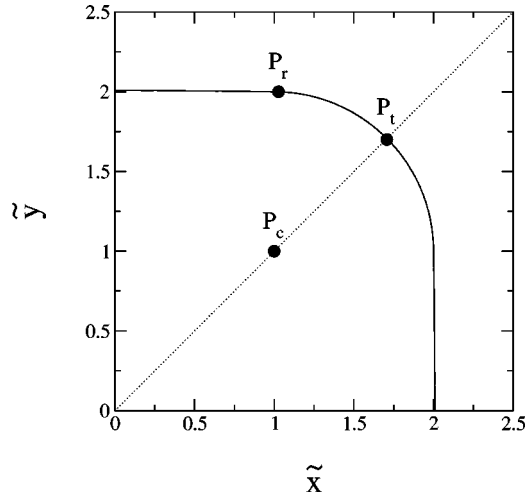
FIG. 2. Analytical equilibrium shape for anisotropy $\delta = 1.0$ and smoothing angle $\theta_0 = \pi/200$. P_r is the rightmost point of the "facet," P_t is the intersection point with the $x = y$ line, and P_c is the center of the arc circle $\widehat{P_r P_t}$.

$$\tau(\theta)\partial_t\psi = [\psi + \lambda\Delta(1-\psi^2)](1-\psi^2) + W(\theta)^2\nabla^2\psi$$
$$+ 2W(\theta)\vec{\nabla}W(\theta)\cdot\vec{\nabla}\psi - (\partial_y\psi)\partial_x[W(\theta)W'(\theta)]$$
$$+ (\partial_x\psi)\partial_y[W(\theta)W'(\theta)]. \tag{33}$$

Initially, the solid is given a circular (or a square) shape and the undercooling is set to $\Delta = \Delta_0$. Time integration of Eq. (33) is performed and the interface velocity along the x axis, V_x, is computed at regular time intervals. If $V_x > 0$, Δ is decreased and it is increased if $V_x < 0$. The increment $\delta\Delta$ is divided by a constant $a > 1$ each time V_x changes sign. This procedure is repeated as long as $\delta\Delta$ is larger than some prescribed value, $\delta\Delta_{min}$. This scheme is known to converge to an equilibrium state [6].

The analytical equilibrium shape is given by

$$\tilde{x} = x(\theta)/R_0 = f_s(\theta)\cos\theta - f'_s(\theta)\sin\theta,$$
$$\tilde{y} = y(\theta)/R_0 = f_s(\theta)\sin\theta + f'_s(\theta)\cos\theta, \tag{34}$$

where $R_0 = d_0/\Delta$ [19]. Let us consider one-eighth of this interface corresponding to $\theta \in [\pi/4, \pi/2]$ (Fig. 2). In the cusp region $\theta \in [\pi/2 - \theta_0, \pi/2]$, one has

$$\tilde{x}(\theta) = B\cos\theta,$$
$$\tilde{y}(\theta) = (B\sin\theta - A), \tag{35}$$

so that the interface is the circle of center $(0, -A)$ and radius B. Since the smoothed cusps are very narrow in practice ($\theta_0 \ll 1$) this circle arc is very flat; it tends to the straight horizontal facet as $\theta_0 \rightarrow 0$. The right end of this interface portion lies at

$$\tilde{x}_r = \tilde{x}(\pi/2 - \theta_0) = B\sin\theta_0,$$
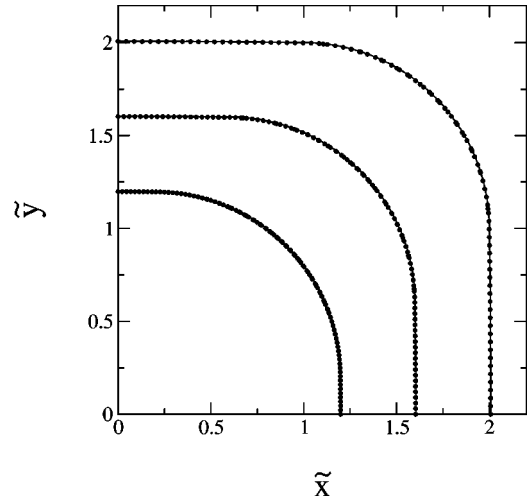$$\tilde{y}_r = \tilde{y}(\pi/2 - \theta_0) = B\cos\theta_0 - A, \tag{36}$$

FIG. 3. Comparison of the analytical equilibrium shape (line) with the phase-field solid-liquid interface (dots) for $\delta = 0.2, 0.5, 1.0$ (from left to right) and $\theta_0 = \pi/200$.

where the local slope is

$$\tilde{y}'_r(\tilde{x}_r) = -\tan\theta_0. \tag{37}$$

On the other hand, for $\theta \in [\pi/4, \pi/2 - \theta_0]$ the crystal is bounded by the circle centered at point $P_c(\delta, \delta)$ (i.e., $x = y = \delta$) of rescaled radius unity, for which

$$\tilde{R} = (\tilde{x}_t - \tilde{x}_r)\sqrt{2} = 1 - \sqrt{2}\sin\theta_0 \tag{38}$$

is a good first-order approximation when $\theta_0 \ll 1$ (Fig. 2).

Note that, as $\theta_0 \rightarrow 0$, one recovers the equilibrium shape for the sharp cusp, with a horizontal facet of length

$$\tilde{\Lambda} = 2\tilde{x}_r \rightarrow 2\delta \tag{39}$$

matching tangentially a circle of rescaled radius unity.

As shown in Fig. 3, the whole crystal shape is well reproduced by the phase-field equilibrium code. A close examination of the numerical data points reveals that the imposed anisotropy is underestimated by about 0.2% in the numerics, independently of θ_0.

B. Numerical estimates for the facet ends

The knowledge of the analytical equilibrium shape guides us to define a numerical procedure to extract estimates of the facet length Λ and corner radius R from discrete interfaces obtained with the phase-field code. On the square mesh, the interface consists in a list of points $P_i(x_i, y_i)$. According to Eq. (37), the two facet ends are located at the points P_r and P_l where the absolute value of the local slope rapidly increases beyond $\tan\theta_0$ (Fig. 4). The method used to compute the two end points is thus to compare the derivative of the equilibrium curve $\partial_x y$ with $\tan\theta_0$. Using centered differences,

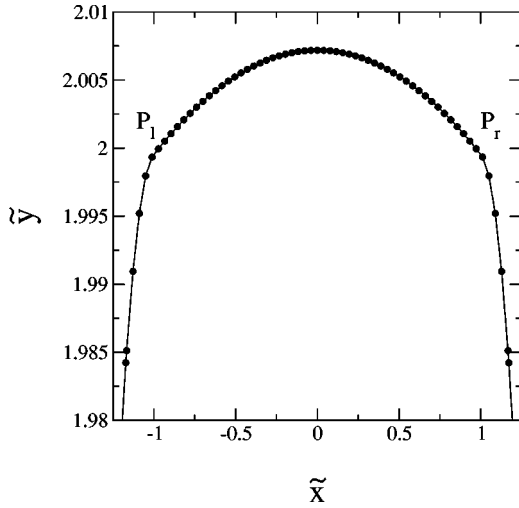$$\partial_x y_i = \frac{y_{i+1} - y_{i-1}}{x_{i+1} - x_{i-1}}, \tag{40}$$

FIG. 4. Closeup of the phase-field equilibrium shape in the region of the smooth facet ($\delta = 1.0$, $\theta_0 = \pi/200$). Dots represent the interface points P_i.

gives an error of about 5% on both measures. On the other hand, using the one-sided approximations

$$\partial_x y_i|^- = \frac{y_i - y_{i-1}}{x_i - x_{i-1}} \tag{41}$$

to compute P_r and

$$\partial_x y_i|^+ = \frac{y_{i+1} - y_i}{x_{i+1} - x_i} \tag{42}$$

to compute P_l, estimates of Λ and R are only 0.5% off the exact values (see Table I). This last estimation procedure is thus more precise and it is readily extended to the case of growth shapes in what follows.

C. Sharp cusp limit

One may still wonder if the sharp cusp limit ($\theta_0 \to 0$) is reachable within our numerical approach. To answer this question, it is better to develop Eq. (33) in terms of the second partial derivatives of ψ. One then gets

$$\tau(\theta) \partial_t \psi = [\psi + \lambda \Delta(1 - \psi^2)](1 - \psi^2)$$
$$+ W_0^2 [C_{xx} \partial_{xx} \psi + C_{xy} \partial_{xy} \psi + C_{yy} \partial_{yy} \psi], \tag{43}$$

TABLE I. Comparison of the facet length (first column) and corner radius (second column) of the equilibrium shape for $\delta = 1.0$ and $\theta_0 = \pi/200$. Analytical values are compared with estimates from phase-field data analyzed with two different interpolation methods.

$\tilde{x}_r - \tilde{x}_l$	$(\tilde{x}_t - \tilde{x}_r)\sqrt{2}$	
1.950	1.034	Centered diff. approx. [Eq. (40)]
2.023	0.983	One-sided approx. [Eqs. (41) and (42)]
2.031	0.978	Analytical

with

$$C_{xx} = \begin{cases} 1 + \delta(3|\cos\theta| - |\cos^3\theta| + |\sin^3\theta|) + \delta^2 \\ A^2 + B^2 - AB|\cos\theta|(2 + \sin^2\theta) \\ B^2 - AB|\sin^3\theta|, \end{cases} \tag{44}$$

$$C_{xy} = \begin{cases} 2\delta(\sigma_s\cos^3\theta + \sigma_c\sin^3\theta) + 2\delta^2\sigma_s\sigma_c \\ -2AB\sigma_c\sin^3\theta \\ -2AB\sigma_s\cos^3\theta, \end{cases} \tag{45}$$

and

$$C_{yy} = \begin{cases} 1 + \delta(3|\sin\theta| - |\sin^3\theta| + |\cos^3\theta|) + \delta^2 \\ B^2 - AB|\cos^3\theta| \\ A^2 + B^2 - AB|\sin\theta|(2 + \cos^2\theta) \end{cases} \tag{46}$$

for $\theta_0 < \theta < \pi/2 - \theta_0$, $\theta \leq \theta_0$, and $\theta \geq \pi/2 - \theta_0$, respectively. The symbols σ_s and σ_c represent the signs (± 1) of $\sin\theta$ and $\cos\theta$.

The time step Δt must be sufficiently small to ensure convergence of the finite-difference scheme, the most stringent constraint on Δt arising for $\theta = \theta_0$:

$$\Delta t \leq \frac{\tau_0}{W_0^2} \frac{h^2}{2} \left[\frac{f_s^2(\theta_0)}{C_{xx}(\theta_0) + C_{yy}(\theta_0)} \right]. \tag{47}$$

As $\theta_0 \ll 1$, this approximates to

$$\Delta t \leq \frac{\tau_0}{W_0^2} \frac{h^2}{2} \left(\frac{1 + \delta}{\delta} \right) \theta_0. \tag{48}$$

It is thus always possible to reduce θ_0 provided that Δt is decreased in proportion. Although Δt depends on the cusp amplitude δ, the time step can still be kept constant while maintaining numerical stability by imposing

$$\theta_0 = K \frac{\delta}{1 + \delta}, \tag{49}$$

with K some constant. In the numerical simulations, we typically take $K = \pi/100$, so that $\Delta t/\tau_0 \leq 0.0025\ldots$. In practice, we rather use the discretization scheme described in Sec. III than the fully developed version given in Eqs. (43)–(46). The former proves to be more precise and more stable than the latter, so that a larger time step $\Delta t/\tau_0 = 0.008$ can be used.

V. FACETED NEEDLE GROWTH

We now turn to nonequilibrium growth shapes. The time evolution of a needle dendrite is illustrated in Fig. 5 for a cusp amplitude $\delta = 1$, diffusion coefficient $D\tau_0/W_0^2 = 4$, and undercooling $\Delta = 0.55$. The size of the simulation box is $600W_0 \times 600W_0$. For reasons of symmetry, it is sufficient to grow one-half of the dendrite (here $y \geq x$). We checked that identical patterns are obtained when the whole quadrant is used. The initial conditions for the phase field are $\psi = 1$ if both $0 \leq x \leq 20W_0$ and $0 \leq y \leq 20W_0$ and $\psi = -1$ otherwise.
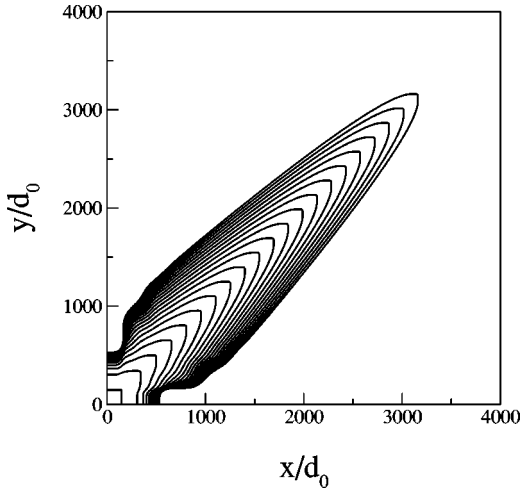
FIG. 5. Time evolution of a faceted dendrite for undercooling $\Delta = 0.55$, smoothing angle $\theta_0 = \pi/200$, and anisotropy $\delta = 1.0$. The time interval between two successive curves is $100\tau_0$.
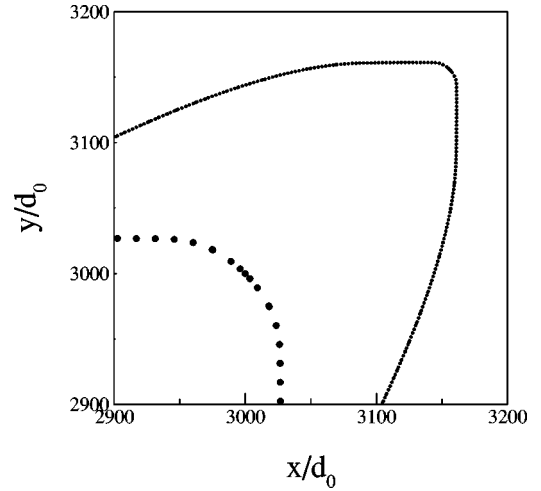

FIG. 6. Enlargement of the foremost dendrite tip of Fig. 5. The tip is further enlarged and shifted to the lower-left corner (larger dots).

This square shape is imposed to the solid germ in order to get a dendrite with a single tip along the $x = y$ direction. Conversely, rounded initial shapes, such as a circle, always result into tip splitting along the growth direction, leading to more complicated patterns which will be discussed later. The temperature field u is initially set to zero inside the solid germ and to $-\Delta$ outside. Reflecting conditions are imposed at all the domain boundaries.

We first focus on the influence of the anisotropy coefficient δ on the dynamics of the faceted needle dendrite. This coefficient is varied from 0.25 to 1.60 in the simulations. After a transient, the dendrite reaches a stationary state which is independent of the size of the initial germ. The tip then moves with a constant velocity V and a rather large portion behind the tip adopts a stable shape. A good test of the thin-interface limit is to decrease independently the rescaled interface thickness W_0/d_0 (or, equivalently, the diffusion coefficient $D\tau_0/W_0^2$) and the grid spacing h/W_0 [6]. Convergence is achieved when the scaled tip velocity $\tilde{V} = Vd_0/D$ is independent of both parameters. Table II shows

that the results are reasonably well converged for the values $D\tau_0/W_0^2 = 4$ and $h/W_0 = 0.4$ used in our simulations.

A. Steady-state shape

The steady-state interface shape can be divided into three distinct parts: a nearly circular tip of radius R, a smooth "facet" of length Λ, and a trailing rough tail (Fig. 6). Estimates of $R = (x_t - x_r)\sqrt{2}$ and $\Lambda = x_r - x_l$ are obtained by using the numerical interpolation method described in Sec. IV B. To smooth out temporal fluctuations, time averages of both quantities are performed over the whole stationary regime. Obviously, the exact shape of the dendrite tip should depend on the smoothing angle θ_0. When θ_0 is sufficiently small this dependence is found to be linear, which allows us to unambiguously extrapolate $R(\theta_0)$ and $\Lambda(\theta_0)$ to $\theta_0 = 0$ (Fig. 7). Up to an overall scale factor, the dendrite tip shape

TABLE II. Convergence of the steady-state tip velocity with decreasing ratio $W_0/d_0 = (D\tau_0)/(a_1 a_2 W_0^2)$ and lattice parameter h/W_0. The other parameters are kept constant, $\Delta = 0.55$, $\delta = 1.0$, $\theta_0 = \pi/200$, and the kinetic coefficient is set to zero.

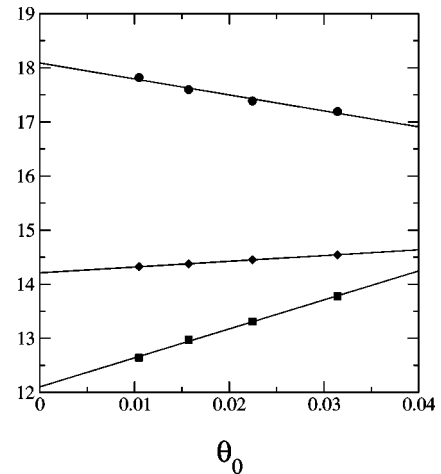| $D\tau_0/W_0^2$	W_0/d_0	h/W_0	$\Delta t/\tau_0$	$V\tau_0/W_0$	Vd_0/D
3	5.42	0.4	0.008	0.158	0.0097
4	7.22			0.285	0.0098
5	9.03			0.402	0.0089
4	7.22	0.2	0.002	0.285	0.0098
		0.4	0.008	0.285	0.0098
		0.6	0.018	0.284	0.0098
		0.8	0.032	0.280	0.0096
		1.0	0.050	0.275	0.0094

FIG. 7. Variations with the smoothing angle θ_0 of R/d_0 (circles), $0.25(\Lambda/d_0)$ (squares), and $50(V\tau_0/W_0)$ (diamonds) for anisotropy $\delta = 1.0$. The continuous lines are linear fits to the data points.
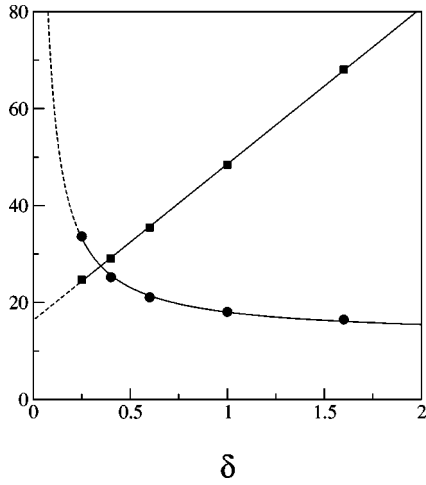
FIG. 8. Variations with the cusp amplitude δ of R/d_0 (circles) and Λ/d_0 (squares). The continuous lines are least-squares fits of the data points to the laws given in Eqs. (50) and (51).

is very similar to the equilibrium shape, i.e., a quarter of a circle matching tangentially to two side facets.

The variations of $\Lambda(0)$ and $R(0)$ with cusp amplitude are displayed in Fig. 8. The results are well fitted by the two simple relations

$$\Lambda = \Lambda_0 \left[1 + \frac{\delta}{\delta_\Lambda} \right] \qquad (50)$$

and

$$R = R_0 \left[1 + \frac{\delta_R}{\delta} \right]. \qquad (51)$$

The asymptotic shape of the trailing rough part away from the facet is well fitted by a parabola that satisfies the Ivantsov relation [20]

$$\Delta = \sqrt{\pi} \sqrt{p} \, e^p \, \mathrm{erfc}(\sqrt{p}) \qquad (52)$$

with the Péclet number

$$p \equiv \frac{\rho V}{2D}. \qquad (53)$$

Note that the reason why the asymptotic tail is a parabola whose tip radius is predicted exactly by the Ivantsov relation is the same as for nonfaceted growth [21,22]. Namely, in a frame that is stationary with respect to the melt, the trailing rough part grows as a planar interface whose position $x(t)$ perpendicular to the growth axis $\sim t^{1/2}$ and the Péclet number $p \equiv x(t)[dx(t)/dt]/2D$ obeys the same relation as Eq. (52), as shown independently of Ivantsov by Zener [23].

We checked in a few simulations that ρV is well predicted by the Ivantsov relation, as illustrated in Fig. 9 where we compare the phase-field interface to the Ivantsov parabola with the same tip velocity, i.e., the parabola with $\rho = 2Dp/V$, where p is the Ivantsov Péclet number and V is the steady-state tip velocity in the phase-field simulation. Given this agreement, we use directly the formula ρ
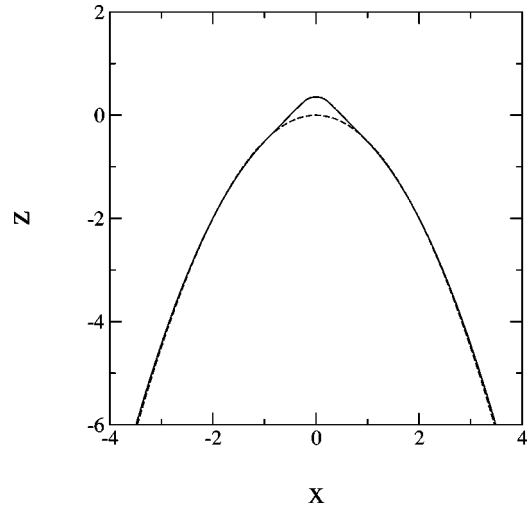

FIG. 9. Same needle dendrite as in Fig. 5 after rotation, translation, and normalization by $\rho = 2Dp/V$ (solid line). Also shown is the corresponding Ivantsov parabola $z = -x^2/2$ (dashed line). Note that here, as in Fig. 17, z represents the main axis of the dendrite, x the axis perpendicular to z, and that both x and z coordinates are normalized by ρ.

$= 2Dp/V$ to calculate ρ in all results reported thereafter. It should be emphasized that the tip radius ρ of this imaginary parabola that matches exactly the asymptotic needle crystal shape and the true tip radius R are quite different as shown in the plot of R/ρ versus δ in Fig. 10. In particular, R/ρ is seen to decrease sharply with increasing δ, while Λ/ρ approaches a constant. These plots reflect the fact that side facets become elongated and extend closer to the tip that becomes more pointed as δ increases.

B. Steady-state operating state

As in previous sharp-interface calculations [16,17], we define the dimensionless tip selection parameter
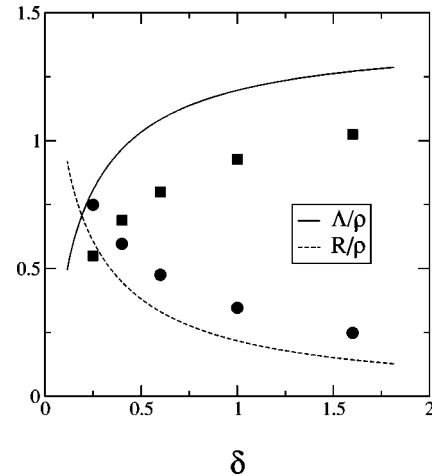

FIG. 10. Plots of Λ/ρ and R/ρ for $\Delta = 0.55$, obtained from phase-field simulations (squares and circles, respectively) and predicted by the sharp-interface theory of Sec. VI (solid and dashed lines, respectively).
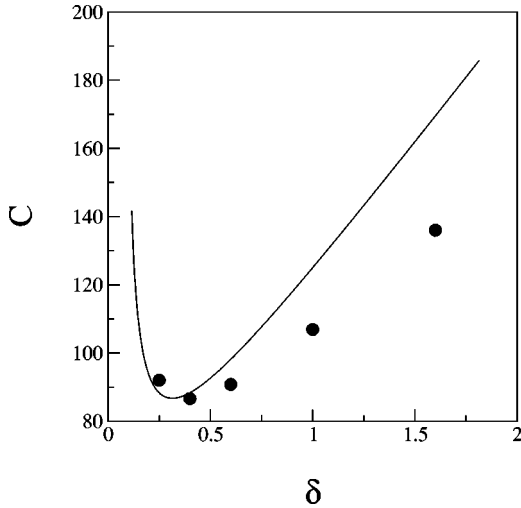
FIG. 11. Tip selection parameter $C = 4\rho^2 V/Dd_0$ vs cusp amplitude δ for $\Delta = 0.55$, extracted from the phase-field simulations (solid circles) and predicted by the approximate sharp-interface analytical theory of Sec. VI (solid line).

$$C \equiv \frac{4\rho^2 V}{Dd_0}, \tag{54}$$

where V is the tip velocity and ρ is the tip radius of the parabola that exactly matches the asymptotic tail of the faceted needle crystal. Note that $C = 8/\sigma$ where $\sigma = 2Dd_0/\rho^2 V$ is the selection parameter that is also often used in dendrite growth studies.

Eliminating ρ in favor of the Péclet number using the relation $\rho = 2Dp/V$, we can rewrite C in the form

$$C = \frac{16D}{Vd_0} p^2. \tag{55}$$

A plot of C versus δ with V corresponding to the steady-state tip velocity in the phase-field simulations and p computed from the Ivantsov relation for the value of Δ corresponding to the simulations is shown in Fig. 11. Note that $C(\delta)$ has a minimum that corresponds to a maximum of tip velocity as a function of δ.

In experiments, the growth rate of a single material is usually studied as a function of undercooling. Additional simulations are thus performed for other values of Δ. All the other parameters are kept constant, except for the total time which is increased to $7000\tau_0$ for $\Delta = 0.45$, $3000\tau_0$ for $\Delta = 0.50$, and reduced to $1500\tau_0$ for $\Delta = 0.60$. We do not extrapolate V to $\theta_0 \rightarrow 0$ here because the computing time becomes prohibitively large for $\Delta < 0.55$. However, from the previous results for $\Delta = 0.55$, we do not anticipate deviations in the tip velocity by more than a few percent (see Fig. 7). The plot of tip velocity versus facet length shown in Fig. 12 shows that our numerical results are consistent with the scaling law $\Lambda \sim V^{-0.5}$, which was found experimentally for NH_4Br needle crystals [14].
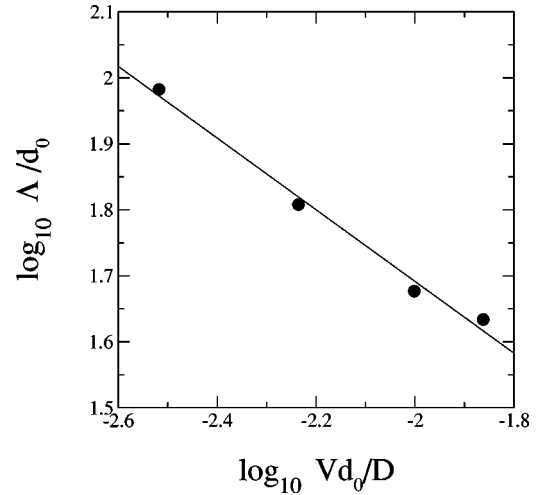

FIG. 12. Log-log plot of the dimensionless facet length Λ/d_0 as a function of the dimensionless tip velocity Vd_0/D for a cusp amplitude $\delta = 1.0$. The straight line is a linear fit to the data points giving a slope -0.54 ± 0.04.

C. Transients

When growth is started from a circular germ, a double needle is systematically observed (Fig. 13), independently of the germ shape, for $\delta \leq 0.20$. Initially, the two tips move away from each other. Our simulations show that these needles ultimately grow practically parallel to each other at very long times, when they are separated from each other by several diffusion lengths (Fig. 13).

At long times, the tip of the double needle becomes comparable in shape to that of the single-needle dendrite (Fig. 14). Of course, the former is thinner on one side because the latent heat accumulates in the channel between the two tips. This similarity in shape suggests that the double-needle pattern is governed by the same operating state as the needle dendrite. Verifying this point with a sufficient accuracy is not easy because of a still longer transient for the double-needle
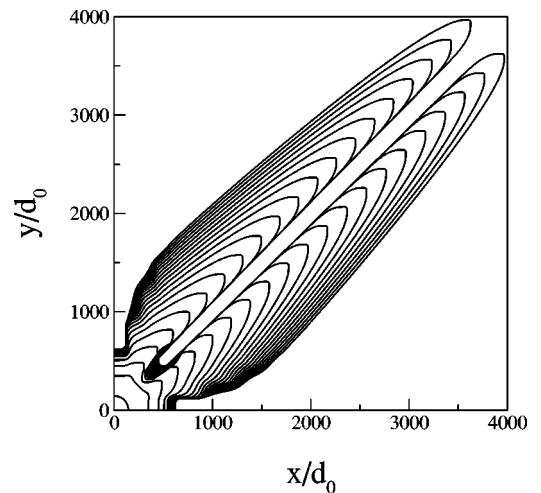

FIG. 13. Time evolution of a double-needle dendrite for undercooling $\Delta = 0.60$ and anisotropy $\delta = 1.0$ (time interval between two contours: $100\tau_0$).
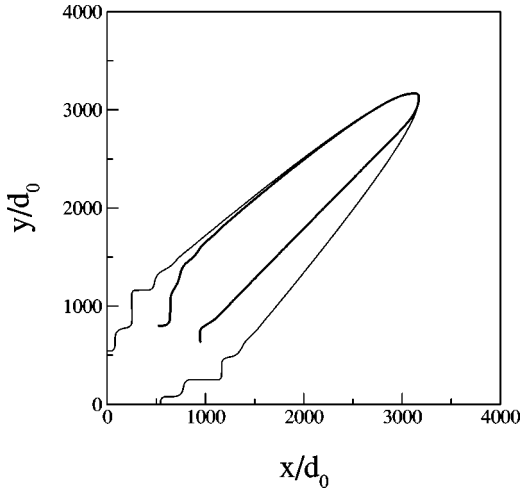
FIG. 14. Comparison between one branch of a double-needle dendrite (thick line) and a single-needle dendrite (thin line). The first curve is shifted to superimpose the two tips. Time $t=1500\tau_0$, undercooling $\Delta=0.60$, and anisotropy $\delta=1.0$.

dendrite. For this reason, we compare the patterns obtained for a larger undercooling, $\Delta=0.60$, for which the simulations are still quantitative but the relaxation time much shorter than with $\Delta=0.55$. After a time $t=2000\tau_0$, the tip velocity of the double-needle pattern has not yet fully converged but it tends slowly to a limit near $0.397W_0/\tau_0$ (Fig. 15). This is precisely the value found for the single-tip dendrite, which confirms that the two asymptotic states are identical. Thus, the double-needle dendrite is merely just a tip-splitting evolution of the single-tip dendrite. This splitting is often preferred by the system because it allows for a more efficient occupation of the available room.

Let us finally remark that the double needle found here is not a faceted version of the generic nonfaceted growth structure that has been termed doublon [24]. Doublons also are symmetry-broken growth shapes with a double tip. However,
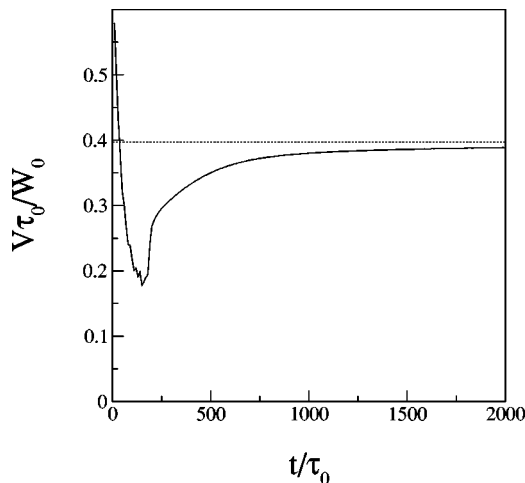

FIG. 15. Tip velocity as a function of time for the double-needle dendrite shown in Fig. 13. The dashed horizontal line gives the stationary velocity obtained for the single-needle dendrite with the same parameters.

the two tips remain much closer than one diffusion length and are thus highly interdependent, which is not true for the double faceted needle dendrite observed in the present simulations.

VI. COMPARISON WITH SHARP-INTERFACE ANALYTICAL THEORY

A precise quantitative comparison of the phase-field results of the last section with previous sharp-interface calculations [16,17] cannot be carried out because these calculations considered the one-sided model with zero diffusivity in the solid phase while we simulated here a symmetric model with equal diffusivities in solid and liquid. In addition, our simulations are for finite Péclet number while the sharp-interface calculations of Refs. [16,17] are restricted to the small Péclet number limit ($p\to 0$). Nonetheless, the phase-field results reproduce several key features of faceted needle growth that were predicted in the sharp-interface studies.

(1) The ratio Λ/ρ of the facet length to the tip radius of the parabola that matches the asymptotic rough tail increases with the cusp amplitude δ and saturates to a value order of unity for large δ.

(2) The tip selection constant C has a minimum for a value of δ of the order of unity. The value of C that corresponds to this minimum is large (~ 100).

(3) For large δ, the needle shape consists of two long facets joined by a nearly circular tip that match on to trailing rough parts that become parabolic far from the tip. This is precisely the shape proposed by Adda Bedia and Hakim [16].

In the remainder of this section, we develop a simple analytical theory of faceted needle growth that is based on the approximate shape proposed by Adda Bedia and Hakim [16] for large δ, where facets are joined by a small circular tip of radius R. We take this approximation further by assuming that (i) it remains valid for δ of the order of unity, and (ii) the trailing rough parts remain parabolic all the way to the points at which they match tangentially the facets, as opposed to being parabolic only asymptotically far from the tip [16]. These simplifications allow us to obtain a simple physical picture of faceted needle growth as well as explicit analytical predictions of the shape parameters R, Λ, and ρ and the velocity V for arbitrary Péclet number, without necessitating the numerical solution of an integral equation as in Refs. [16,17]. As we shall see below, these predictions agree reasonably well with our phase-field results despite our simple parametrization of the steady-state shape.

The complete determination of the needle shape (R, Λ, and ρ) and the growth velocity V for fixed Δ and δ requires four independent relations. The first is the Ivantsov relation (52) that fixes the product ρV. A second relation between R, Λ, and ρ is simply obtained by imposing that the circular tip and parabolic tails match tangentially the front and trailing ends of the facets, respectively, which yields at the relation

$$\rho=(\Lambda+R)/\sqrt{2}. \qquad (56)$$

We can check this relation by comparing the tip velocity in the phase-field simulations with the velocity $V=2Dp/\rho$,
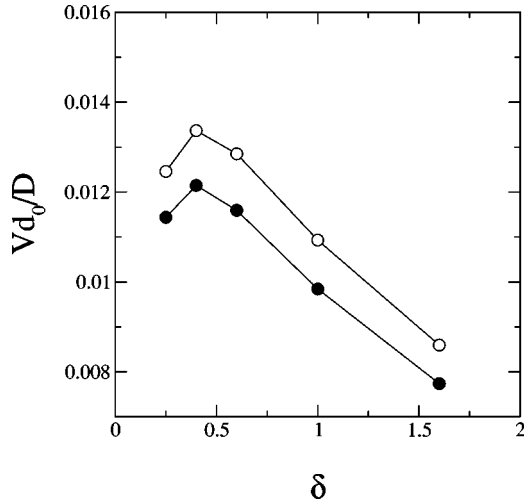
FIG. 16. Variation of dimensionless tip velocity Vd_0/D with cusp amplitude δ obtained from the phase-field simulations for $\Delta = 0.55$ (solid circles) and using the equation $V = 2Dp/\rho$, where $p(\Delta)$ is the Péclet number predicted by the Ivantsov relation, and $\rho = (\Lambda + R)/\sqrt{2}$, where Λ and R are the facet length and tip radius obtained from the phase-field shapes (empty circles).

where p is the Péclet number predicted by the Ivantsov relation and ρ is computed using Eq. (56) together with values of Λ and R in the simulations. Figure 16 shows that these two velocities are in reasonably good quantitative agreement. The systematic deviation is most likely due to the fact that the crystal tail is not exactly parabolic very close to the facet.

The two other relations needed to complete our theory are obtained by imposing the Gibbs-Thomson condition (3) at the tip of the needle crystal and by using the integral form of this condition on the facet [Eq. (5)]. For this, we need an expression for the undercooling along the interface that is obtained straightforwardly using the known boundary integral relation [25,26]

$$u(x) = -\Delta + p \int_{-\infty}^{+\infty} \frac{dx'}{\pi} \exp\{-p\,[z(x) - z(x')]\}$$
$$\times K_0(p\,\sqrt{(x-x')^2 + [z(x) - z(x')]^2}), \qquad (57)$$

where K_0 is the zeroth-order modified Bessel function, p is given by the Ivantsov relation (52), and $z(x)$ is the interface shape with length in unit of ρ. For a circular tip and parabolic tails matching tangentially side facets that make a 45° angle with respect to the growth axis, the x coordinates of the front and trailing ends of the facets are $x = \pm R/\sqrt{2}\rho$ and $x = \pm 1$, and

$$z = \left(\frac{R^2}{\rho^2} - x^2\right)^{1/2} - \frac{\sqrt{2}R}{\rho} + \frac{1}{2}, \quad 0 \leqslant |x| \leqslant \frac{R}{\sqrt{2}\rho}, \quad (58)$$

$$z = -|x| + \frac{1}{2}, \qquad \frac{R}{\sqrt{2}\rho} \leqslant |x| \leqslant 1, \qquad (59)$$
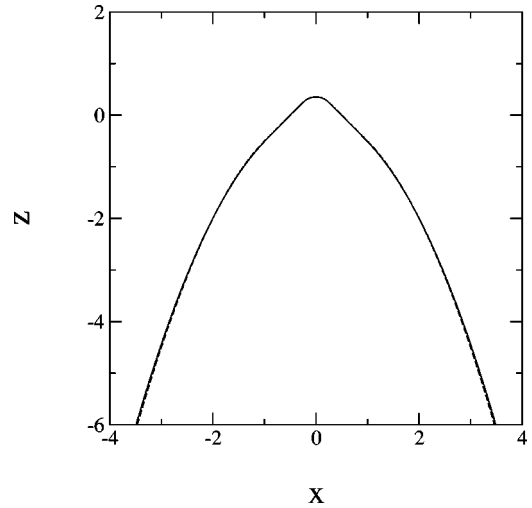

FIG. 17. Comparison of the phase-field needle dendrite of Fig. 9 (solid line) with the faceted needle crystal shape assumed in the analytical theory with a circular tip and a parabolic tail (dashed line). Both curves are for the same parameter value $R/(\sqrt{2}\rho) = 0.25$.

$$z = -\frac{x^2}{2}, \qquad |x| \geqslant 1. \qquad (60)$$

These equations describe rather accurately the phase-field needle dendrites (Fig. 17). Since the isothermal Ivantsov parabola is an exact solution of the steady-state growth problem without capillarity, the integral relation (57) is exactly satisfied for $z = -x^2/2$ and $u = 0$. In contrast, as illustrated in Fig. 9, the tip of the faceted needle crystal protrudes ahead of the tip of this parabola and hence is undercooled by a finite amount $u(0)$. The Gibbs-Thomson condition (3) imposes a relation between this tip undercooling and the tip radius that is simply

$$u(0) = -d_0/R. \qquad (61)$$

In turn, Eq. (5) provides us with a relation between the average undercooling on the facet and the cusp amplitude δ that takes the form here

$$\sqrt{2} \int_{R/\sqrt{2}\rho}^{1} dx\, u(x) = -2\frac{d_0}{\rho}\delta, \qquad (62)$$

where x is in units of ρ as above. The four relations defined by Eqs. (52), (56), (61), and (62), together with the expression for u on the interface defined by Eqs. (57)–(60), completely determine R, Λ, ρ, and V. Since the product ρV is exactly predicted by the Ivantsov relation, we only need to compute three independent dimensionless combinations of the four above quantities to compare the predictions of the above theory with the phase-field results. The most meaningful dimensionless combinations are the selection parameter C and the two ratios Λ/ρ and R/ρ. To compute those as a function of δ, it is convenient to vary R/ρ and compute C, δ, and Λ/ρ using the following relations that are simple to deduce:

$$\delta = \frac{\rho}{\sqrt{2}\,u(0)R} \int_{R/\sqrt{2}\rho}^{1} dx\, u(x), \tag{64}$$

$$\frac{\Lambda}{\rho} = \sqrt{2}\left(1 - \frac{R}{\sqrt{2}\rho}\right). \tag{65}$$

The above predictions are compared with the phase-field results in Figs. 10 and 11. The quantitative agreement between the two is reasonably good but not exact because the steady-state shape that we have assumed here differs slightly from the true shape (Fig. 17) that is only exactly parabolic asymptotically far from the facet.

To conclude, we note that the expression for $u(x)$ can be simplified in the small Péclet number limit where Eq. (57) reduces to [27]

$$u(x) = -p \int_{-\infty}^{+\infty} \frac{dx'}{2\pi} \ln\left[\frac{(x-x')^2 + [z(x) - z(x')]^2}{(x-x')^2 + (x'^2/2 - x^2/2)^2}\right]. \tag{66}$$

Therefore, both $u(0)$ and the integral of $u(x)$ along the facet are simply proportional to the Péclet number in this limit and hence C, R/ρ, and Λ/ρ are only functions of δ. Furthermore, it is straightforward to deduce that $\Lambda/\rho \to \sqrt{2}$, $R/\rho \to 0$, and $C \sim \delta$ in the large δ limit. Hence this theory predicts the scaling law $\Lambda \sim V^{-1/2}$ that is a simple consequence of the fact that Λ/ρ and $C \sim \rho^2 V$ are constants in the small Péclet number limit.

VII. CONCLUDING REMARKS

In conclusion, we have shown that the phase-field approach can be successfully extended to model the solidification of faceted materials. Our approach, which consists of rounding the cusps in the γ plot, converges well in the limit of sharp cusps for both equilibrium and nonequilibrium growth shapes with facets. Even though we have considered a simple form of the γ plot, the method should be applicable to more complex γ plots where the interface stiffness varies on the rough parts.

In addition, we have developed an approximate analytical theory of faceted needle growth that includes capillarity and assumes circular and parabolic forms for the front and trailing rough parts of steady-state needle crystals, respectively. This theory yields explicit predictions of tip velocity and facet length that are in good overall quantitative agreement

with the phase-field results; this agreement is largely due to the fact that the needle shape assumed in the theory is a very good approximation to the actual growth shape observed in the phase-field simulations. Furthermore, this theory predicts that the scaling law $\Lambda \sim V^{-1/2}$ observed both experimentally [14] and in the present phase-field simulations should hold in the small Péclet number limit, consistent with the results of previous theoretical studies [15–17].

In the present study, we have established a quantitative comparison between phase-field and sharp-interface results under the assumption that the variation of interface undercooling is dominated by capillarity. Using scaling arguments, Ben Amar and Pomeau [15] have concluded that, under the assumption that the growth of facets is dominated by a Franck-Read screw dislocation mechanism, the $\Lambda \sim V^{-1/2}$ scaling law still holds. While growth conditions where kinetic effects are negligible may exist, we suspect that such effects will generally be important in the presence of facets, as widely believed. Therefore, a quantitative incorporation of facet kinetics in a phase-field model remains an important task for the future. The phase-field model as formulated thus far reproduces a linear relationship between the planar interface velocity and interface undercooling appropriate for a rough interface. On facets, however, standard growth mechanisms such as screw dislocations or ledge nucleation lead to a nonlinear relationship between velocity and undercooling. These relationships could potentially be incorporated in the phase-field model by letting the kinetic relaxation time τ depend on temperature or supersaturation, in addition to orientation.

Another interesting future prospect is to model the directional solidification of alloys with faceted interfaces [28–30] by combining the present methodology to handle cusped γ plots with a recent thin-interface phase-field formulation of alloy solidification [9].

---

[1] J.S. Langer, in *Directions in Condensed Matter* (World Scientific, Singapore, 1986), p. 164.

[2] J.B. Collins and H. Levine, Phys. Rev. B **31**, 6119 (1985).

[3] For recent reviews, see W.J. Boettinger, J.A. Warren, C. Beckermann, and A. Karma, Annu. Rev. Mater. Sci. **32**, 163 (2002); A. Karma, in *Encyclopedia of Materials: Science and Technology*, edited by K.H.J. Buschow, R.W. Cahn, M.C. Flemings, B. Ilschner, E.J. Kramer, and S. Mahajan (Elsevier, Oxford, 2001), pp. 6873–6886, Vol. 7.

[4] A.A. Wheeler, B.T. Murray, and R. Schaefer, Physica D **66**, 243 (1993).

[5] S-L. Wang and R.F. Sekerka, Phys. Rev. E **53**, 3760 (1996).

[6] A. Karma and W.J. Rappel, Phys. Rev. E **53**, R3017 (1996); **57**, 4323 (1998).

[7] N. Provatas, N. Goldenfeld, and J. Dantzig, Phys. Rev. Lett. **80**, 3308 (1998); J. Comput. Phys. **148**, 265 (1999).

[8] M. Plapp and A. Karma, Phys. Rev. Lett. **84**, 1740 (2000); J. Comput. Phys. **165**, 592 (2000).

[9] A. Karma, Phys. Rev. Lett. **87**, 115701 (2001).

[10] J.J. Eggleston, G.B. McFadden, and P.W. Voorhees, Physica D **150**, 91 (2001).

[11] K.A. Jackson, in *Liquid Metals and Solidification* (ASM, Cleveland, Ohio), p. 174.

[12] D.P. Woodruff, *The Solid-Liquid Interface* (Cambridge University Press, London, 1983).

[13] J.P. Franck and J. Jung, Physica D **23**, 259 (1986).

[14] J. Maurer, P. Bouissou, B. Perrin, and P. Tabeling, Europhys. Lett. **8**, 67 (1989).

[15] M. Ben Amar and Y. Pomeau, Europhys. Lett. **6**, 609 (1988).

[16] M. Adda Bedia and V. Hakim, J. Phys. I **4**, 383 (1994).

[17] M. Adda Bedia and M. Ben Amar, Phys. Rev. E **51**, 1268 (1995).

[18] D.A. Porter and K.E. Easterling, *Transformations in Metals and Alloys* (Chapman and Hall, London, 1992), p. 114.

[19] P.W. Voorhees, S.R. Coriell, G.B. McFadden, and R.F. Sekerka, J. Cryst. Growth **67**, 425 (1984).

[20] G.P. Ivantsov, Dokl. Akad. Nauk SSSR **58**, 567 (1947).

[21] E. Brener, Phys. Rev. Lett. **71**, 3653 (1993).

[22] A. Karma, in *Branching in Nature*, Proceedings of the Les Houches Winter School, Vol. 14, edited by V. Fleury, J.F. Gouyet, and M. Léonetti (EDP Sciences, Les Ulis, 2001), Chap. XI, pp. 365–401.

[23] C. Zener, J. Appl. Phys. **20**, 950 (1949).

[24] T. Ihle and H. Müller-Krumbhaar, Phys. Rev. E **49**, 2972 (1994).

[25] G.E. Nash and M.E. Glicksman, Acta Metall. **22**, 1283 (1974).

[26] A. Barbieri and J.S. Langer, Phys. Rev. A **39**, 5314 (1989).

[27] P. Pelcé and Y. Pomeau, Stud. Appl. Math. **74**, 245 (1986).

[28] L.M. Fabietti and R. Trivedi, Metall. Trans. A **22A**, 1249 (1991); J. Cryst. Growth **162**, 185-197 (1997).

[29] N. Dey and J.A. Sekhar, Acta Metall. Mater. **41**, 409 (1993).

[30] B. Billia, D. Benielli, N. Bergeon, Y. Dabo, R. Guérin, H. Jamgotchian, H. Nguyen Thi, and P. Voge, in *Proceedings of the International Conference on Solidification Science and Processing: Outlook for the 21st Century*, edited by B.K. Dhindaw, B.S. Murty, and S. Sen (Science, Enfield, NH, 2001), p. 25.